

H3DE-Net: Efficient and Accurate 3D Landmark Detection in Medical Imaging

Zhen Huang^{1,2}, Ronghao Xu^{3,4}, Xiaoqian Zhou^{3,4}, Yangbo Wei^{1,5},
Suhua Wang⁶, Xiaoxin Sun⁷, Han Li⁸, Qingsong Yao⁹

¹School of Computer Science and Technology, University of Science and Technology of China (USTC), Hefei, 230026, China.

²School of Information Science and Technology, Eastern Institute of Technology (EIT), Ningbo, 315200, China.

³School of Biomedical Engineering, Division of Life Sciences and Medicine, USTC, Suzhou, 215123, China.

⁴Suzhou Institute for Advanced Research, USTC, Suzhou, 215123, China.

⁵Shanghai Jiao Tong University, Shanghai, 200030, China.

⁶Computer Department, Changchun Humanities and Sciences College, Changchun, 130117, China.

⁷School of Information Science and Technology, Northeast Normal University, Changchun, 130117, China.

⁸Computer Aided Medical Procedures (CAMP), School of Computation, Information and Technology, Technische Universitaet Muenchen (TUM), Germany.

⁹Stanford University, California, 94305, United States.

Abstract

3D landmark detection is a critical task in medical image analysis, and accurately detecting anatomical landmarks is essential for subsequent medical imaging tasks. However, mainstream deep learning methods in this field struggle to simultaneously capture fine-grained local features and model global spatial relationships, while maintaining a balance between accuracy and computational efficiency. Local feature extraction requires capturing fine-grained anatomical details, while global modeling requires understanding the spatial relationships within complex anatomical structures. The high-dimensional nature of 3D volume further exacerbates these challenges, as landmarks are sparsely distributed, leading to

significant computational costs. Therefore, achieving efficient and precise 3D landmark detection remains a pressing challenge in medical image analysis. In this work, We propose a **Hybrid 3D DEtection Net**(H3DE-Net), a novel framework that combines CNNs for local feature extraction with a lightweight attention mechanism designed to efficiently capture global dependencies in 3D volumetric data. This mechanism employs a hierarchical routing strategy to reduce computational cost while maintaining global context modeling. To our knowledge, H3DE-Net is the first 3D landmark detection model that integrates such a lightweight attention mechanism with CNNs. Additionally, integrating multi-scale feature fusion further enhances detection accuracy and robustness. Experimental results on a public CT dataset demonstrate that H3DE-Net achieves state-of-the-art(SOTA) performance, significantly improving accuracy and robustness, particularly in scenarios with missing landmarks or complex anatomical variations. We already open-source our project, including code, data and model weights on <https://github.com/ECNUACRush/H3DE-Net>.

Keywords: 3D Landmark Detection, Medical Image Analysis, Transformer-CNN Hybrid Model.

1 Introduction

3D landmark detection is a critical task in medical image analysis, with wide applications [3, 14, 27, 29, 39, 46, 48, 58] in surgical navigation [38], disease diagnosis [9, 50, 53], and treatment planning [7]. Compared to 2D landmark detection, 3D landmark detection is more challenging due to the increased complexity of volumetric data [5, 33, 56]. For example, 3D medical imaging modalities such as CT scans contain rich anatomical structures but exhibit larger data volumes, more intricate spatial geometries, and significant patient-specific variability. Furthermore, landmarks in 3D images are often sparsely distributed and subject to low signal-to-noise ratio (SNR) and resolution differences. These factors make 3D landmark detection particularly difficult, especially in scenarios involving complex anatomical structures or missing landmarks.

Traditional marking methods mainly depend on manual annotations and rule-based algorithms. Although these approaches were significant in the early stages of medical image processing, they also present clear limitations. Firstly, rule-based algorithms often depend on specific image features, making it challenging to adapt to diverse medical images or complex lesions [20–22]. Secondly, the manual annotation process is time-consuming and susceptible to subjective influences, resulting in inconsistencies and inaccuracies in the annotations.

Convolutional neural networks (CNNs) have become the mainstream approach for 3D landmark detection, driven by rapid advances in deep learning [1, 10, 12, 18, 30–32, 52]. CNNs excel at extracting hierarchical and multi-scale features, making them practical for analyzing complex medical images. In particular, their ability to capture local spatial patterns is advantageous in tasks requiring detailed anatomical information. However, CNNs have limited receptive fields and struggle to model long-range dependencies, which are crucial for accurately detecting sparsely distributed landmarks in

3D. This lack of global context modeling represents a significant bottleneck for further performance improvement.

Transformer architectures [45], such as Vision Transformers (ViT) [6] and Swin Transformers, have gained traction in 3D medical imaging due to their ability to capture long-range dependencies through self-attention mechanisms [17, 24, 25, 35, 54]. This feature addresses the limitations of CNNs, which struggle with global context representation. Consequently, hybrid architectures that integrate CNNs for local feature extraction and lightweight Transformers for global context are emerging as effective solutions. This approach can better meet the dual demands of fine-grained spatial representation and holistic understanding in 3D landmark detection. However, the high computational cost and storage requirements of these hybrid models, along with the larger data volume and complexity of 3D data compared to 2D, hinder the performance of existing models, preventing them from achieving optimal results.

To tackle these challenges, we propose a hybrid framework, **Hybrid 3D DEtection Network (H3DE-Net)**, which integrates CNNs and lightweight Transformer modules for robust and accurate 3D landmark detection. Specifically, CNNs are utilized for efficient local feature extraction and multi-scale representation, while a Transformer module equipped with a bi-level routing attention mechanism enhances global context modeling. We also introduce a Feature Fusion Module (FFM) that integrates multi-scale features, effectively capturing global and local dependencies. This synergistic design enables H3DE-Net to overcome the limitations of standalone architectures and achieve precise and reliable landmark detection even in challenging scenarios.

Our main contributions are summarized as follows:

- We propose a hybrid CNN-Transformer model, **H3DE-Net**, for 3D landmark detection. By combining CNNs for local feature extraction with a lightweight attention mechanism for global context modeling, the model achieves state-of-the-art (SOTA) performance in challenging scenarios.
- We design a feature fusion module (FFM) for multiscale feature integration to restore fine-grained spatial details, significantly enhancing the precision and robustness of landmark detection.
- Extensive experiments on the public CT dataset demonstrate that our method outperforms existing baselines across multiple metrics, particularly in scenarios involving complex anatomical structures and missing landmarks.

2 Related Work

2.1 Landmark Detection in Medical Imaging

Landmark detection is a fundamental task in medical image analysis, aimed at identifying anatomically significant feature points essential for ensuring the reliability and interpretability of automated systems [49].

Early landmark detection methods relied on hand-crafted features [20–22] and model-based approaches. Cootes et al. [16] introduced Active Shape Models (ASM), which employed statistical shape constraints to guide landmark localization, requiring

significant manual intervention but achieving moderate success in capturing anatomical variations. Active Appearance Models (AAM) [37] extended ASM by incorporating texture characteristics, improving accuracy in anatomical structure detection. These traditional approaches heavily relied on feature engineering, with methods such as SIFT [23] for extracting transformation-invariant features and rule-based techniques [8, 34] for detecting edges and contours using geometric features and prior knowledge. However, these methods often struggled with anatomical variability, image quality degradation, and noise, limiting their robustness in clinical applications.

Deep learning, particularly CNNs and U-Net variants [13, 14, 36, 39, 44], revolutionized landmark detection through hierarchical feature learning. These architectures excel at capturing multi-scale features and have demonstrated remarkable success in various medical imaging tasks. Payer et al. [32] developed a stacked hourglass network for iterative refinement and deep regression networks that combined heatmap prediction with coordinate regression. Extended 3D heatmap-based approaches [10, 52] have further advanced the field by effectively processing volumetric data and providing robust spatial predictions. While these methods show promising results in 3D landmark detection, they face inherent limitations in capturing long-range dependencies and global context, mainly when modeling complex volumetric anatomical relationships across different planes.

2.2 Hybrid CNN-Transformer Model

Recent advances in Transformer architectures have shown promising potential in addressing CNNs' limitations in capturing long-range dependencies. Vision Transformers [6] excel at modeling global context through self-attention mechanisms, complementing CNNs' local feature extraction capabilities. This complementary nature has led to the development of hybrid CNN-Transformer architectures, particularly in medical image analysis. Models such as TransUNet [2] and nnFormer [57] and others [15, 17, 24, 25, 28, 35, 40, 41, 43, 54] integrate Transformer modules into U-Net frameworks to enhance feature representation, demonstrating significant improvements in capturing spatial dependencies across different anatomical regions. Landmark detection has particularly benefited from this architectural advancement, with approaches like SpineHRFormer [55] and DATR [59] leveraging the combined strengths of both architectures. These hybrid models have demonstrated superior performance by capturing fine-grained anatomical details through CNN features and modeling long-range structural relationships via self-attention mechanisms, effectively addressing the limitations of traditional CNN-based approaches.

However, extending these hybrid approaches to 3D landmark detection faces significant challenges. The quadratic computational complexity of self-attention mechanisms concerning input size makes direct application to volumetric data prohibitive. At the same time, the increased dimensionality of 3D data demands substantial computational resources and training data. These limitations highlight the need for more efficient architectural designs tailored for 3D landmark detection tasks.

3 Method

3.1 Problem Definition

This study focuses on detecting anatomical landmarks around teeth and surrounding structures in head 3D-CT scans. Given a 3D medical image volume $I \in \mathbb{R}^{D \times H \times W}$, the goal is to predict the 3D coordinates of N landmarks, denoted as $L = \{l_1, l_2, \dots, l_N\}$, where each landmark is represented as $l_i = (x_i, y_i, z_i)$.

We formulate the detection task as a heatmap regression problem to localize landmarks. For each landmark l_i , its location in 3D space is represented by a Gaussian distribution. The corresponding heatmap is defined as:

$$H_i(x, y, z) = \exp\left(-\frac{(x - x_i)^2 + (y - y_i)^2 + (z - z_i)^2}{2\sigma^2}\right), \quad (1)$$

where (x_i, y_i, z_i) is the ground-truth coordinate of the i -th landmark, and σ controls the spread of the Gaussian distribution. The final heatmap H is the summation of all individual landmark heatmaps: $H = \sum_{i=1}^N H_i$.

During inference, the predicted coordinate of each landmark \hat{l}_i is obtained by finding the peak value in the predicted heatmap:

$$\hat{l}_i = (\hat{x}_i, \hat{y}_i, \hat{z}_i) = \arg \max_{(x, y, z)} H(x, y, z), \quad (2)$$

3.2 3D BiFormer Design

The 3D BiFormer Module is the core component of H3DE-Net, designed to efficiently extract global and local features from 3D data. By extending the BiFormer module [60] from 2D to 3D, the module introduces a bi-level routing attention mechanism, significantly reducing computational complexity while maintaining the ability to model long-range dependencies and local details. The module’s structure, shown in Figure 1(a), consists of the following key components:

- Depthwise Convolution (DWConv): Captures local spatial features.
- Bi-Level Routing Attention: Dynamically models global and local dependencies, consisting of Region-to-Region Routing and Token-to-Token Attention.
- Layer Normalization (LN) and Multi-Layer Perceptron (MLP): Optimize feature distributions and enhance feature representations.

3.2.1 Bi-Level Routing Attention Mechanism

The Bi-level routing attention mechanism, illustrated in Figure 1(b), operates in two stages:

Region-to-Region Routing

In this stage, the input feature $F \in \mathbb{R}^{H \times W \times D \times C}$ is divided into multiple regions. For each region, coarse-grained attention is computed using the query Q^p and key K^p .

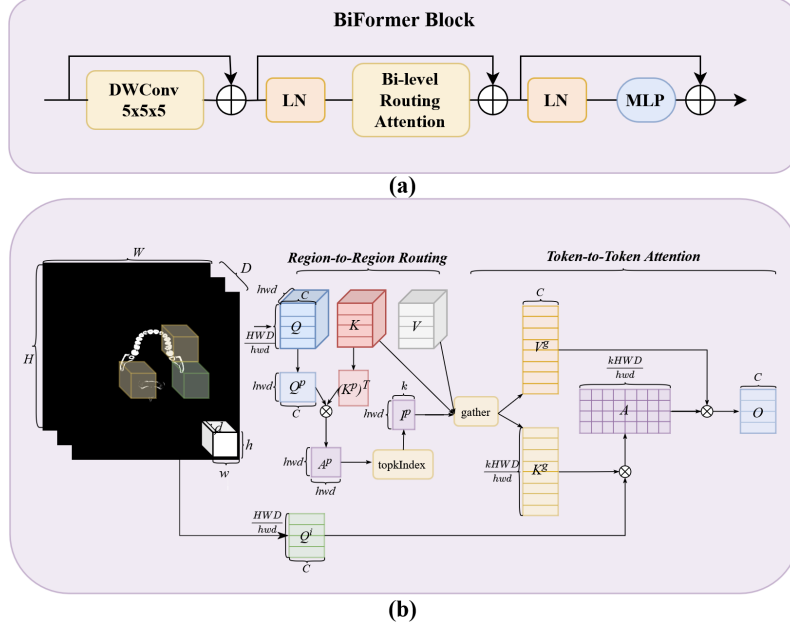


Fig. 1 (a) Architecture of the proposed BiFormer Block. (b) Illustration of region-to-region routing and token-to-token attention. Our method uses sparsity by selecting key-value pairs from the top- k most relevant windows, avoiding unnecessary calculations.

The coarse-grained attention is defined as:

$$\text{Attention}_{\text{coarse}}(Q^p, K^p) = \text{Softmax} \left(\frac{Q^p (K^p)^\top}{\sqrt{d_k}} \right), \quad (3)$$

where $Q^p, K^p \in \mathbb{R}^{(h \times w \times d) \times C}$ are extracted from F , h, w, d represent the local region dimensions, and d_k is the attention head dimension.

The results of coarse-grained routing are used to select high-relevance regions via a Top- k selection mechanism **topkIndex**, producing a set of region indices, which reduces the computational burden of the subsequent steps.

Token-to-Token Attention

Within the selected regions, fine-grained attention is computed to capture detailed features. The computation is defined as:

$$\text{Attention}_{\text{fine}}(Q^*, K^*, V^*) = \text{Concat}(\text{head}_1, \dots, \text{head}_h) W_O, \quad (4)$$

where $Q^*, K^*, V^* \in \mathbb{R}^{k \times d_k}$ are the features of the selected tokens, k is the number of selected tokens, W_O is a linear projection matrix, and head_i represents each independent attention head.

Finally, the aggregated attention within the regions produces the output features $O \in \mathbb{R}^{H \times W \times D \times C}$.

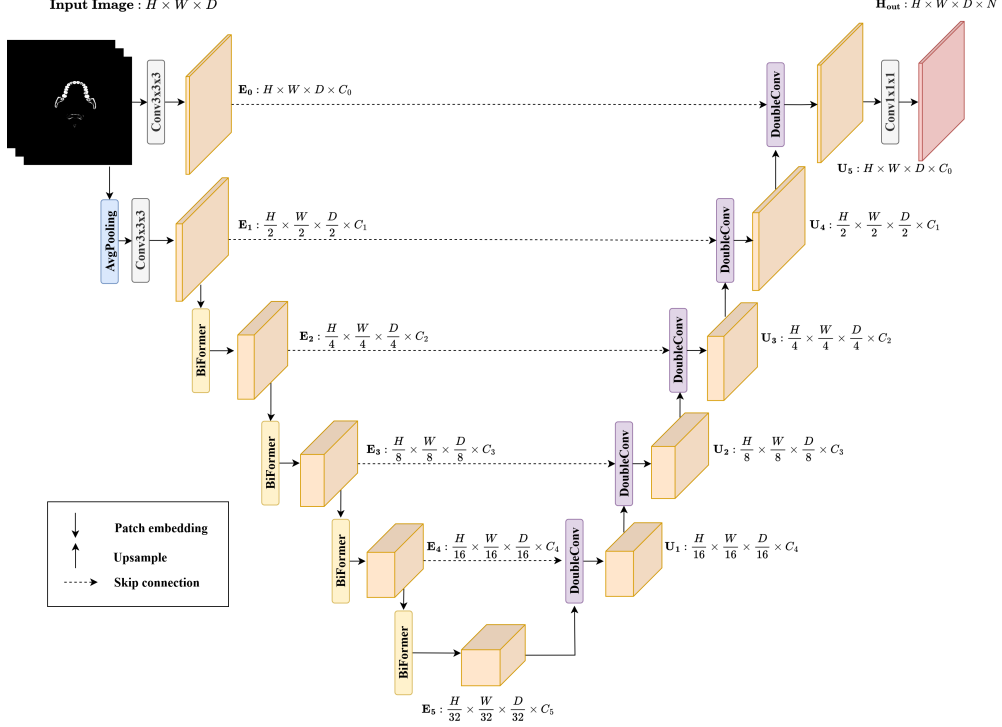


Fig. 2 The overview of proposed Hybrid-3D Detection Network(H3DE-Net): Anchor-Free Architectures. BiFormer is a module based on bilevel routing attention, and DoubleConv stands for two Cascading convolution layers. Further details will be discussed later. N denotes the number of landmarks.

3.3 Designed Architectures

To accommodate different task requirements(We cover this in detail in Sec. 4.1), we design two architectures: **Anchor-Free Architecture** and **Anchor-Based Architecture**. Both architectures follow a unified encoder-decoder framework, employ the 3D BiFormer module for multi-scale feature extraction, and integrate additional components such as the **Feature Fusion Module (FFM)**. These components further enhance the model’s capability to aggregate multi-scale information and recover spatial details, which is critical for accurate landmark localization.

3.3.1 Anchor-Free Architecture

As shown in Fig. 2, the Baseline architecture directly generates a 3D heatmap $H_{out} \in \mathbb{R}^{H \times W \times D \times L}$, where H, W, D represent the spatial dimensions of the input image, and L is the total number of landmarks. The network achieves global modeling of landmarks through progressive encoding, decoding, and feature fusion.

Given a 3D input image $I \in \mathbb{R}^{H \times W \times D}$, an initial convolution layer first extracts embedded features:

$$E_0 = \text{Conv}_{3 \times 3}(I), \quad E_0 \in \mathbb{R}^{H \times W \times D \times C_0}. \quad (5)$$

The encoder then extracts multi-scale features $E_i \in \mathbb{R}^{\frac{H}{2^i} \times \frac{W}{2^i} \times \frac{D}{2^i} \times C_i}$ ($i = 1, 2, \dots, 5$) through successive 3D BiFormer modules:

$$E_i = \text{BiFormer}(E_{i-1}), \quad i = 1, 2, \dots, 5. \quad (6)$$

As the feature maps progress through the encoder, their spatial resolution decreases while the number of channels increases, facilitating the extraction of higher-level abstract features. The decoder gradually restores the spatial resolution through upsampling layers U_j ($j = 1, 2, \dots, 4$), which are combined with skip connections from the encoder to enhance the information flow:

$$U_j = \text{Fusion}(U_{j+1}, E_{5-j}), \quad j = 1, 2, \dots, 4. \quad (7)$$

The fusion process is implemented through the Feature Fusion Module (FFM), which concatenates the upsampled features from the previous stage with the corresponding encoded features:

$$U_j = \text{Concat}(\text{Deconv3D}(U_{j+1}), E_{5-j}). \quad (8)$$

Finally, the decoder produces a heatmap H_{out} through a $1 \times 1 \times 1$ convolution:

$$H_{\text{out}} = \text{Conv}_{1 \times 1 \times 1}(U_1), \quad H_{\text{out}} \in \mathbb{R}^{H \times W \times D \times L}. \quad (9)$$

This architecture is characterized by its simplicity and direct modeling of global landmark distributions through heatmaps. It is well-suited for tasks where landmarks are regularly distributed and data is complete. By leveraging global modeling, the Baseline architecture effectively utilizes full-image information, avoiding local deviations that might affect predictions.

3.3.2 Anchor-Based Architecture

Figure 3 illustrates the anchor design, which addresses the issue of missing landmarks in the dataset. Anchors are uniformly distributed in a grid layout across the 3D feature space, with fixed intervals and radii r . Each anchor serves as a candidate for predicting landmark positions through offset regression and existence probability estimation. The offset regression is parameterized as:

$$t_x = \frac{g_x - f_x}{r}, \quad t_y = \frac{g_y - f_y}{r}, \quad t_z = \frac{g_z - f_z}{r}, \quad (10)$$

where (g_x, g_y, g_z) are the ground-truth coordinates of the landmark, (f_x, f_y, f_z) are the anchor center coordinates, and r is the anchor radius. The two subfigures in Figure 3 demonstrate different anchor configurations.

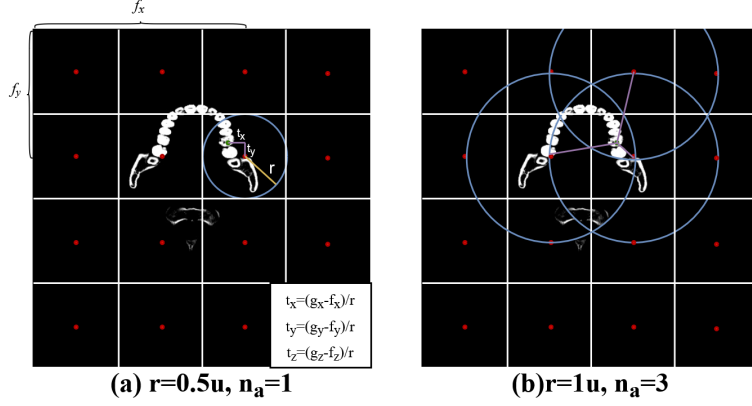


Fig. 3 (a) shows a single-scale anchor design where $r = 0.5u$ and the number of anchors $n_a = 1$, while (b) shows a multi-scale anchor design where $r = 1u$ and $n_a = 3$. The multi-scale design enhances the coverage of regions surrounding partially missing landmarks, making the model more robust in handling irregular landmark distributions and incomplete data.

The Anchor-Based architecture introduces an anchor proposal mechanism that divides the 3D space into candidate regions and predicts the offsets and probabilities for each anchor. As shown in Figure 4, the architecture consists of an encoder and a decoder. The encoder extracts multi-scale features from the input 3D image $H \times W \times D$ using the 3D BiFormer module. Each encoder stage generates feature maps E_i with progressively reduced spatial dimensions:

$$E_i = \text{BiFormer}(E_{i-1}), \quad i = 1, 2, \dots, 5, \quad (11)$$

where $E_i \in \mathbb{R}^{\frac{H}{2^i} \times \frac{W}{2^i} \times \frac{D}{2^i} \times C_i}$.

The decoder reconstructs spatial resolution through upsampling layers and skip connections. The final decoder stage outputs U_1 , which is used to generate two prediction branches: 1) An offset regression branch that predicts the offsets Δl of each anchor relative to the ground-truth landmark positions:

$$\Delta l = f_{\text{offset}}(U_1), \quad \Delta l \in \mathbb{R}^{\frac{H}{4} \times \frac{W}{4} \times \frac{D}{4} \times (3 \cdot L)}, \quad (12)$$

where L is the number of landmarks, and the factor of 3 corresponds to the x, y, and z coordinates in 3D space. 2) A probability prediction branch that estimates the existence probability p of a landmark for each anchor. The probabilities are normalized using the sigmoid activation function σ :

$$p = \sigma(f_{\text{prob}}(U_1)), \quad p \in \mathbb{R}^{\frac{H}{4} \times \frac{W}{4} \times \frac{D}{4} \times L}. \quad (13)$$

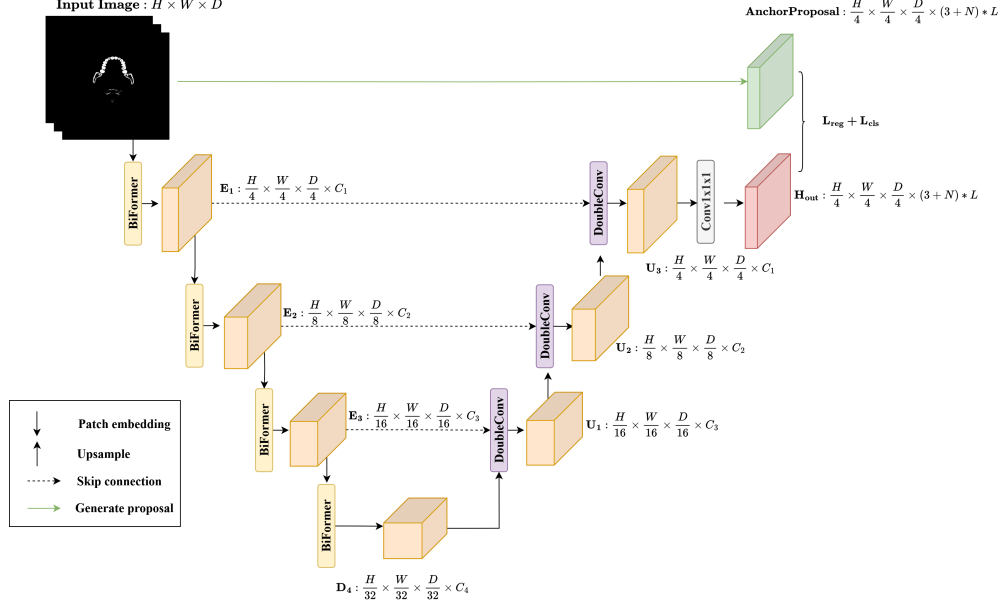


Fig. 4 The overview of proposed Hybrid-3D Network(H3DE-Net): Anchor-Based Architectures.

By focusing on candidate regions, the Anchor-Based architecture captures landmark-specific local features more accurately, making it particularly effective for scenarios with irregularly distributed or missing landmarks.

3.4 Loss Function

The network is optimized using a hybrid loss function tailored to the architecture. For the Anchor-free architecture, the loss is based solely on the heatmap regression, while for the Anchor-based architecture, additional anchor-related terms are included.

The heatmap regression loss, applicable to both architectures, is defined as:

$$\mathcal{L}_{\text{heatmap}} = \frac{1}{HWDN} \sum_{n=1}^N \sum_{h=1}^H \sum_{w=1}^W \sum_{d=1}^D (H(h, w, d, n) - G(h, w, d, n))^2, \quad (14)$$

where $H(h, w, d, n)$ and $G(h, w, d, n)$ are the predicted and ground truth heatmap values for the n -th landmark at voxel (h, w, d) . H, W, D , and N represent the spatial dimensions and number of landmarks.

The anchor regression loss is:

$$\mathcal{L}_{\text{reg}} = \frac{1}{N} \sum_{i=1}^N \|(\Delta x_i, \Delta y_i, \Delta z_i) - (\hat{\Delta x}_i, \hat{\Delta y}_i, \hat{\Delta z}_i)\|^2, \quad (15)$$

where $(\Delta x_i, \Delta y_i, \Delta z_i)$ and $(\hat{\Delta x}_i, \hat{\Delta y}_i, \hat{\Delta z}_i)$ are the ground truth and predicted offsets for the i -th anchor.

The classification loss is:

$$\mathcal{L}_{\text{cls}} = -\frac{1}{N} \sum_{i=1}^N [p_i \log \hat{p}_i + (1 - p_i) \log(1 - \hat{p}_i)], \quad (16)$$

where p_i and \hat{p}_i are the ground truth and predicted existence probabilities for the i -th anchor.

For the Anchor-free architecture, the total loss is:

$$\mathcal{L}_{\text{total}} = \mathcal{L}_{\text{heatmap}}. \quad (17)$$

For the Anchor-based architecture, the total loss combines anchor regression, classification, and heatmap regression terms:

$$\mathcal{L}_{\text{total}} = \lambda_{\text{reg}} \mathcal{L}_{\text{reg}} + \lambda_{\text{cls}} \mathcal{L}_{\text{cls}} + \lambda_{\text{heatmap}} \mathcal{L}_{\text{heatmap}}. \quad (18)$$

Here, λ_{reg} and λ_{cls} are hyperparameters that control the contributions of the anchor-related loss terms.

4 Experiment

4.1 Dataset Preprocessing and Evaluation Metric

Dataset: We evaluate the performance of **H3DE-Net** using the publicly available 3D skull landmark detection dataset from [10]. The dataset includes 658 CT scans (458 / training, 100 / validation, 100 / testing), each carefully annotated with 14 anatomical landmarks for the mandibular molar landmarking (MML) task. This task aims to identify the anatomical positions of the crowns and roots of mandibular molars. The dataset is systematically categorized into two distinct subsets to facilitate more comprehensive evaluations: **Complete Cases** and **Incomplete Cases**.

The Complete Cases subset contains CT scans in which all 14 landmarks are thoroughly annotated. This subset consists of 283 training volumes, 56 validation volumes, and 60 test volumes. In contrast, the Incomplete Cases subset introduces additional complexity, as some landmarks are missing due to various factors such as occlusion, reduced image quality, or imaging artifacts. This incomplete subset comprises 175 volumes for training, 44 for validation, and 40 for testing. This subset is particularly significant because it reflects the challenges encountered in real-world clinical scenarios, where datasets are often incomplete and affected by noise. Incomplete cases serve as a critical aspect of the evaluation process, testing the robustness and adaptability of the model to ambiguous or missing data.

Preprocessing Steps: To prepare CT images for training and evaluation, we implement a series of pre-processing steps designed to standardize the input data, reduce computational complexity, and enhance the robustness of the model through data augmentation. These steps are described in detail below:

Firstly, the voxel intensity is normalized to all CT images. The raw intensity values, which can vary significantly between different scans due to variations in imaging protocols and acquisition devices, are normalized to $[0, 255]$. This normalization step ensures consistency in input data, allowing the model to focus on anatomical features rather than being influenced by imaging artifacts or variations in intensity scaling.

Secondly, we perform random cropping of the input volumes to accommodate GPU memory limitations and maintain computational efficiency. Each CT image is cropped to a fixed size of $128 \times 128 \times 64$ voxels. This strategy reduces the overall computational cost and ensures that the model can process input volumes efficiently during training and inference. The random cropping process introduces some variability in the spatial positioning of anatomical structures within the input data, which helps the model learn more generalized feature representations.

Evaluation Metric: Recent studies have used voxel Euclidean distance (VED), mean radial error (MRE), successful detection rate (SDR), and root mean square error (RMSE) as criteria for evaluating models. MRE and SDR are widely used and considered standard metrics for 3D cephalometric landmark detection. Therefore, our evaluation metrics use MRE and SDR with standard deviation. The MRE represents the average Euclidean distance between the predicted and true values, while the SDR measures the accuracy of the detected landmarks at different distances, especially at 2 mm, 2.5 mm, 3 mm, and 4 mm. The formulas for these metrics are as follows:

$$MRE = \frac{1}{n} \sum_{i=1}^n \sqrt{\sum_{\tau \in \{x, y, z\}} ((g_{\tau}^i - f_{\tau}^i) \cdot (s_{\tau}^i)^2)}, \quad (19)$$

$$SDR = \frac{\text{number of accurate detections}}{\text{number of detections}} \times 100\%, \quad (20)$$

In this landmark detection task using CT dental data, n represents the total number of data points. g_{τ}^i denotes the ground truth value of the i -th landmark for the coordinate axis τ (where $\tau \in \{x, y, z\}$), which corresponds to the true location of the dental landmarks in the CT data. f_{τ}^i is the predicted value of the i -th landmark for the coordinate axis τ , which corresponds to the predicted location of the dental landmarks. s_{τ}^i is the scaling factor for the i -th point in the coordinate axis τ , adjusting for the spacing or resolution of the CT data.

4.2 Baseline Methods

To rigorously validate the effectiveness and robustness of **H3DE-Net**, we conduct a comprehensive performance comparison against several baseline methods widely recognized in the field of medical image analysis. The methods included in the comparison are as follows:

- **UNet3D [4]:** UNet is a basic encoder-decoder method that skips connections is widely used in heat-map-based landmark detection. UNet3D is an improved 3D version of UNet for MRI and CT images.
- **VNet [26]:** VNet replaces pooling layers with convolutional layers for downsampling, uses transposed convolution to restore resolution, and adds horizontal residual connections to address the vanishing gradient problem. It excels in medical imaging and 3D object segmentation tasks.
- **ResUNet3D [19]:** ResUNet is one of the most important improved versions of UNet, replacing U-Net’s original encoder with ResNet. It combines the advantages of ResNet and U-Net, effectively addressing the vanishing gradient problem and the loss of semantic information.
- **HRNet [42]:** A widely recognized method in landmark detection, HRNet has achieved significant success. This paper evaluates two configurations, HRNet-32 and HRNet-48.
- **SRPose [47]:** SRPose is a super-resolution head for human pose estimation, showing significant improvements in landmark detection accuracy.
- **MTL [51]:** MTL (Multi-task Learning) integrates landmark detection with tasks like bone segmentation, leveraging shared spatial information. Zhang et al. [51] propose a context-guided fully convolutional neural network using displacement maps to learn spatial information, enabling simultaneous completion of both tasks.
- **Two-Stage [11]:** Recent works decompose landmark detection into successive sub-tasks for simplification. He et al. [11] propose a two-phase framework: the first stage uses a global detection network (GDN) to generate candidate landmarks, and the second stage employs a local refinement network (LRN) to refine landmark locations by processing image blocks. This two-stage approach balances performance and computation.
- **SRLD-UNet & SR-UNet [52]:** Zhang et al. propose two super-resolution landmark detection networks, SRLD-Net and SR-UNet, to improve accuracy and reduce errors in medical imaging.

4.3 Experimental Results

4.3.1 Quantitative Results

To evaluate the performance of **H3DE-Net** and compare it to these baseline methods, experiments are conducted on three dataset configurations: 1) *complete dataset*, which only includes complete cases where all landmarks are fully annotated; there are no missing landmarks in this dataset, so Anchor-free Architecture is not needed; 2) *incomplete dataset*, which only includes incomplete cases where some landmarks are missing due to occlusion, imaging artifacts, or other factors. On such datasets, Anchor-Based Architecture is used because the landmarks are missing; 3) *all cases dataset*, which combines complete and incomplete cases to evaluate the generalization ability of the model in different scenarios. In this kind of data set, because some of the landmarks are missing, Anchor-Based Architecture is used.

Table 1 summarizes the quantitative results of **H3DE-Net** compared with the baseline methods including **VNet**, **UNet3D** and **ResUNet3D**. On *complete dataset*,

H3DE-Net achieves an MRE of $1.68 \pm 0.45\text{mm}$ and a SDR of 97.02% at a threshold of 4mm. It significantly exceeds the strongest baseline **UNet3D**, which has an MRE of $1.90 \pm 0.65\text{mm}$ and an SDR (4mm) of 93.54%. Experimental results show that the proposed model has high accuracy when dealing with noiseless data.

Table 1 The experimental results for VNet, UNet3D, ResUNet3D, and H3DE-Net. We train on the All, Complete, and Incomplete datasets, and test on the same sets. “✓” indicates the use of an anchor, while “✗” indicates no anchor is used.

Networks	Datasets	Anchor	MRE \pm Std (mm)	SDR (%)			
				2 mm	2.5 mm	3 mm	4 mm
VNet [26]	All	✓	1.82 ± 0.73	71.72	83.50	90.07	94.95
	Complete	✗	1.99 ± 0.71	67.86	78.31	85.20	91.20
	Incomplete	✓	2.59 ± 1.82	49.19	64.05	75.68	90.54
UNet3D [4]	All	✓	1.77 ± 0.87	73.97	85.21	91.98	96.45
	Complete	✗	1.90 ± 0.65	65.94	77.81	86.99	93.54
	Incomplete	✓	2.26 ± 1.26	61.89	74.86	82.43	91.89
ResUNet3D [19]	All	✓	1.70 ± 0.72	76.43	86.45	90.91	95.20
	Complete	✗	1.96 ± 0.82	70.03	79.97	86.10	92.73
	Incomplete	✓	2.29 ± 1.44	58.65	72.79	81.08	89.46
H3DE-Net(Ours)	All	✓	1.67 ± 0.64	76.03	86.50	92.31	96.69
	Complete	✗	1.68 ± 0.45	71.19	85.24	91.67	97.02
	Incomplete	✓	2.07 ± 0.96	64.55	76.61	85.29	93.72

On the All Cases dataset, **H3DE-Net** maintained good performance, with MRE reaching $1.67 \pm 0.64\text{mm}$. This is a significant improvement over the three baselines. In addition, at the 2mm and 4mm thresholds, SDR reaches 76.03% and 96.69%, respectively, while **ResUNet3D** reaches 76.43% and 95.20%, respectively. These results highlight the ability of the model to effectively generalize on heterogeneous datasets, capturing anatomical variations without sacrificing accuracy.

Even under the challenging *incomplete dataset* configuration, where missing landmarks and imaging artifacts make the localization task very difficult, **H3DE-Net** shows robust performance. Its MRE is $2.07 \pm 0.96\text{mm}$, and SDR (4mm) is 93.72%, which are better than **UNet3D**’s MRE of $2.26 \pm 1.26\text{mm}$ and SDR (4mm) of 91.89%. These findings highlight the robustness of H3DE-Net, especially when incomplete data introduces ambiguity.

In addition to the above three baseline methods, we also compare the performance of H3DE-Net with several competitive methods, including HRNet-32, HRNet-48, SRPose, Two-Stage, MTL, SRLD-UNet, and SR-UNet; we conduct experiments on the All training dataset. Table 2 summarizes the results in terms of MRE and SDR at thresholds of 2 mm, 2.5 mm, 3 mm, and 4 mm.

Among all comparison methods, H3DE-Net demonstrates excellent performance across all metrics, showcasing its advantages in accuracy and robustness. Specifically, compared to HRNet-32 and HRNet-48, H3DE-Net reduced MRE by 36.74% and

Table 2 The performance comparison between H3DE-Net and other SOTA methods. We extract the results from [52], where ‘-’ indicates that the result is not presented.

Networks	MRE \pm Std (mm)	SDR (%)			
		2 mm	2.5 mm	3 mm	4 mm
HRNet-32 [42]	2.64 \pm 5.18	60.81	–	82.27	90.22
HRNet-48 [42]	2.77 \pm 5.83	58.89	–	82.05	90.16
SRPose [47]	2.58 \pm 5.73	70.09	–	87.27	92.46
Two-Stage [11]	1.78 \pm 0.81	68.93	82.48	88.68	95.37
MTL [51]	1.91 \pm 0.75	69.70	80.47	87.29	93.86
SRLD-UNet [52]	2.40 \pm 5.63	74.98	–	90.39	94.45
SR-UNet [52]	2.01 \pm 4.33	76.14	–	92.02	95.84
H3DE-Net(Ours)	1.67 \pm 0.64	76.03	86.50	92.31	96.69

39.71%, respectively, while improving SDR (4 mm) by 6.47% and 6.53%. Although the Two-Stage method performs relatively better in MRE (1.78 \pm 0.81 mm), it lagged behind H3DE-Net in SDR (2 mm) and SDR (3 mm) by 7.10% and 3.63%, respectively, indicating H3DE-Net’s stronger advantages in high-precision detection scenarios.

Additionally, compared to the MTL method, H3DE-Net reduces MRE by 12.57% and improves the detection success rate in SDR (4 mm) by 2.83%, further validating its generalization ability across different task scenarios. Notably, compared to SRPose and SRLD-UNet, H3DE-Net significantly improves all SDR metrics, especially at the challenging 2 mm detection threshold, where it increases by 5.94% and 1.59%, respectively, demonstrating its superiority in detecting small-range errors.

These experimental results indicate that H3DE-Net’s excellence stems from its innovative network architecture, which effectively captures multi-scale features and fuses global and local information, achieving higher accuracy and robustness in complex data. Compared to traditional networks, H3DE-Net has achieved SOTA performance in the current task through efficient modeling of deep features and adaptive handling of missing or noisy data.

Overall, the results demonstrate the consistent superiority of H3DE-Net across all dataset configurations. The proposed method not only outperforms baseline models under ideal conditions but also excels in real-world scenarios where incomplete or heterogeneous data is prevalent. These findings validate the robustness and versatility of the proposed framework, establishing it as a reliable tool for landmark localization tasks in medical imaging.

4.3.2 Qualitative Results

We visually analyze the experimental results as follows. The ground truth landmark positions are represented in green, and the predicted landmark positions are represented in red. To ensure clear visibility, we remove some voxels to prevent obstructing the landmarks.

Figure 5 shows the visualization results of three Anchor-Based methods and H3DE-Net using all training data. Figure 6 shows the results of three Anchor-Based methods on the complete dataset.

It can be observed that H3DE-Net consistently achieves superior localization accuracy, especially in anatomically intricate regions such as the nasal cavity and the skull

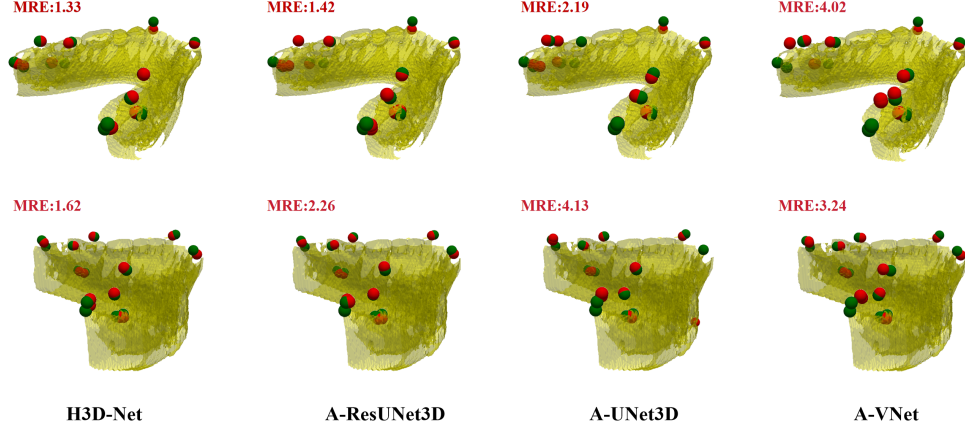


Fig. 5 Landmark detection performance of H3DE-Net train and test on the all datasets. The prefix 'A-' represents the Anchor-Based method, and the way anchors are added is the same as shown in Fig. 4.

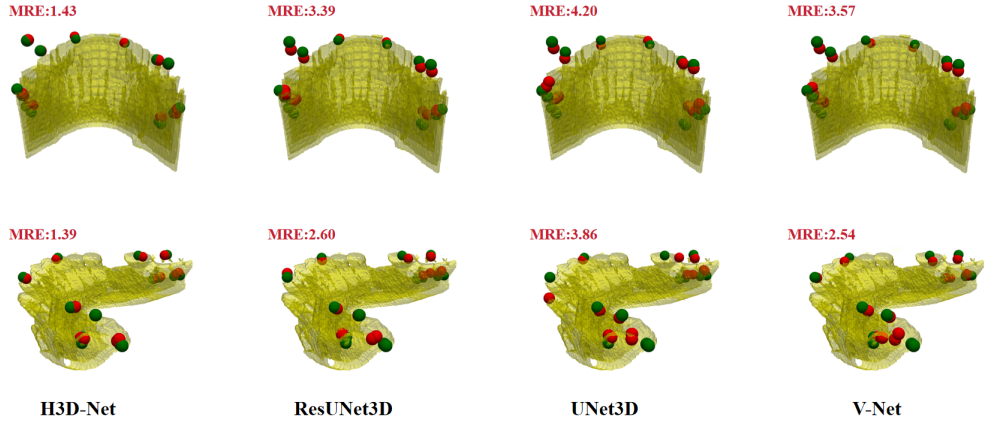


Fig. 6 Landmark detection performance of H3DE-Net train and test on the complete datasets.

base. These regions are characterized by high structural variability and proximity to adjacent anatomical landmarks, making them particularly challenging for baseline models. In comparison, baseline methods often show significant deviations in these areas, leading to errors that are visually apparent in the overlay of predicted and ground truth landmarks. Specifically, H3DE-Net has the following advantages:

- **Higher Local Accuracy:** In regions with complex anatomical structures, such as the skull base, H3DE-Net significantly reduces the deviation between predicted points and ground truth points. In contrast, models like VNet and UNet tend to overfit to incomplete or noisy data in these areas, leading to deviations in

predicted locations. H3DE-Net accurately aligns predictions with true anatomical landmarks. As evident from visual overlays, the proposed method achieves more precise predictions around ground truth points.

- **Enhanced Robustness:** Compared to baseline models, H3DE-Net demonstrates superior robustness when handling incomplete cases caused by missing or occluded landmarks. Specifically, even in the absence of certain anatomical cues, H3DE-Net can accurately predict key point locations. This is attributed to its effective utilization of both global and local contextual information, ensuring high prediction stability in complex scenarios.

5 Conclusion

This paper proposes H3DE-Net, a novel hybrid framework for 3D landmark detection in medical images. By combining the strengths of CNNs and Transformers, the model effectively addresses the challenges of volumetric data, such as sparse landmark distribution, complex anatomical structures, and multi-scale dependencies. The CNN backbone ensures efficient local feature extraction and multi-scale representation, while the 3D BiFormer module leverages a bi-level routing attention mechanism to efficiently model global context with reduced computational overhead. Additionally, integrating the feature fusion module further enhances the model’s robustness and precision. Extensive experiments on a public dataset demonstrate that H3DE-Net significantly outperforms existing methods, achieving state-of-the-art accuracy and robustness. The proposed model excels in challenging scenarios, such as missing landmarks or complex anatomical variations, making it a promising approach for real-world clinical applications.

Future work will explore further optimization of computational efficiency and model scalability to address even larger datasets and more diverse imaging modalities. Moreover, the potential of extending the framework to multi-task learning scenarios, such as combining landmark detection with segmentation or registration, offers exciting opportunities for advancing medical image analysis.

References

- [1] Ao, Y., Wu, H.: Feature aggregation and refinement network for 2d anatomical landmark detection. *Journal of Digital Imaging* **36**(2), 547–561 (2023)
- [2] Chen, J., Lu, Y., Yu, Q., Luo, X., Adeli, E., Wang, Y., Lu, L., Yuille, A.L., Zhou, Y.: Transunet: Transformers make strong encoders for medical image segmentation. *arXiv preprint arXiv:2102.04306* (2021)
- [3] Chowdhury, A.A., Mahmud, S.H., Hoque, K.K.S., Ahmed, K., Bui, F.M., Lio, P., Moni, M.A., Al-Zahrani, F.A.: Stackfbas: Detection of fetal brain abnormalities using cnn with stacking strategy from mri images. *Journal of King Saud University-Computer and Information Sciences* **35**(8), 101647 (2023)
- [4] Çiçek, Ö., Abdulkadir, A., Lienkamp, S.S., Brox, T., Ronneberger, O.: 3d u-net: learning dense volumetric segmentation from sparse annotation. In: *Medical Image Computing and Computer-Assisted Intervention–MICCAI 2016: 19th*

- International Conference, Athens, Greece, October 17-21, 2016, Proceedings, Part II 19. pp. 424–432. Springer (2016)
- [5] Cui, L., Liu, B., Xu, G., Guo, J., Tang, W., He, T.: A pseudo-3d coarse-to-fine architecture for 3d medical landmark detection. *Neurocomputing* **614**, 128782 (2025)
 - [6] Dosovitskiy, A.: An image is worth 16x16 words: Transformers for image recognition at scale. arXiv preprint arXiv:2010.11929 (2020)
 - [7] Gallego, P., Ambroa, E., PérezAlija, J., Jornet, N., Anson, C., Tejedor, N., Vivancos, H., Ruiz, A., Barceló, M., Dominguez, A., et al.: Breast radiotherapy planning: A decision-making framework using deep learning. *Medical Physics* (2024)
 - [8] Grau, V., Alcaniz, M., Juan, M., Monserrat, C., Knoll, C.: Automatic localization of cephalometric landmarks. *Journal of Biomedical Informatics* **34**(3), 146–156 (2001)
 - [9] Hao, W., Liu, S., Lv, C., Wang, Y., Wang, J.: Efficient and privacy-preserving multi-party skyline queries in online medical primary diagnosis. *Journal of King Saud University-Computer and Information Sciences* **35**(8), 101637 (2023)
 - [10] He, T., Xu, G., Cui, L., Tang, W., Long, J., Guo, J.: Anchor ball regression model for large-scale 3d skull landmark detection. *Neurocomputing* **567**, 127051 (2024)
 - [11] He, T., Yao, J., Tian, W., Yi, Z., Tang, W., Guo, J.: Cephalometric landmark detection by considering translational invariance in the two-stage framework. *Neurocomputing* **464**, 15–26 (2021). <https://doi.org/https://doi.org/10.1016/j.neucom.2021.08.042>, <https://www.sciencedirect.com/science/article/pii/S0925231221012261>
 - [12] Hsu, G.S., Shie, H.C., Hsieh, C.H., Chan, J.S.: Fast landmark localization with 3d component reconstruction and cnn for cross-pose recognition. *IEEE Transactions on Circuits and Systems for Video Technology* **28**(11), 3194–3207 (2017)
 - [13] Huang, Z., Li, H., Shao, S., Zhu, H., Hu, H., Cheng, Z., Wang, J., Kevin Zhou, S.: Pele scores: pelvic x-ray landmark detection with pelvis extraction and enhancement. *International Journal of Computer Assisted Radiology and Surgery* **19**(5), 939–950 (2024)
 - [14] Huang, Z., Wang, S., Hu, H., Xu, Y.: Retigan: A hybrid image enhancement method for medical images. In: 2024 5th International Conference on Computer Vision, Image and Deep Learning (CVIDL). pp. 25–29. IEEE (2024)
 - [15] Jiang, H., Chen, Q., Wang, R., Du, J., Chen, T.: Swformer: a scale-wise hybrid cnn-transformer network for multi-classes weed segmentation. *Journal of King Saud University-Computer and Information Sciences* **36**(7), 102144 (2024)
 - [16] Keustermans, J., Mollemans, W., Vandermeulen, D., Suetens, P.: Automated cephalometric landmark identification using shape and local appearance models. In: 2010 20th International Conference on Pattern Recognition. pp. 2464–2467. IEEE (2010)
 - [17] Khan, S., Fazil, M., Sejwal, V.K., Alshara, M.A., Alotaibi, R.M., Kamal, A., Baig, A.R.: Bichat: Bilstm with deep cnn and hierarchical attention for hate speech detection. *Journal of King Saud University-Computer and Information Sciences* **34**(7), 4335–4344 (2022)

- [18] Lee, H., Park, M., Kim, J.: Cephalometric landmark detection in dental x-ray images using convolutional neural networks. In: Medical imaging 2017: Computer-aided diagnosis. vol. 10134, pp. 494–499. SPIE (2017)
- [19] Lee, K., Zung, J., Li, P., Jain, V., Seung, H.S.: Superhuman accuracy on the snemi3d connectomics challenge. arXiv preprint arXiv:1706.00120 (2017)
- [20] Lindner, C., Bromiley, P.A., Ionita, M.C., Cootes, T.F.: Robust and accurate shape model matching using random forest regression-voting. *IEEE transactions on pattern analysis and machine intelligence* **37**(9), 1862–1874 (2014)
- [21] Liu, D., Zhou, K.S., Bernhardt, D., Comaniciu, D.: Search strategies for multiple landmark detection by submodular maximization. In: 2010 IEEE computer society conference on computer vision and pattern recognition. pp. 2831–2838. IEEE (2010)
- [22] Lowe, D.G.: Object recognition from local scale-invariant features. In: Proceedings of the seventh IEEE international conference on computer vision. vol. 2, pp. 1150–1157. Ieee (1999)
- [23] Lowe, D.G.: Object recognition from local scale-invariant features. In: Proceedings of the seventh IEEE international conference on computer vision. vol. 2, pp. 1150–1157. Ieee (1999)
- [24] Lu, X., Yang, R., Zhou, J., Jiao, J., Liu, F., Liu, Y., Su, B., Gu, P.: A hybrid model of ghost-convolution enlightened transformer for effective diagnosis of grape leaf disease and pest. *Journal of King Saud University-Computer and Information Sciences* **34**(5), 1755–1767 (2022)
- [25] Lu, Y., Fan, X., Wang, J., Chen, S., Meng, J.: Parau-net: An improved unet parallel coding network for lung nodule segmentation. *Journal of King Saud University-Computer and Information Sciences* **36**(9), 102203 (2024)
- [26] Milletari, F., Navab, N., Ahmadi, S.A.: V-net: Fully convolutional neural networks for volumetric medical image segmentation. In: 2016 fourth international conference on 3D vision (3DV). pp. 565–571. Ieee (2016)
- [27] Mostafiz, R., Uddin, M.S., Reza, M.M., Rahman, M.M., et al.: Covid-19 detection in chest x-ray through random forest classifier using a hybridization of deep cnn and dwt optimized features. *Journal of King Saud University-Computer and Information Sciences* **34**(6), 3226–3235 (2022)
- [28] Nizamani, A.H., Chen, Z., Nizamani, A.A., Bhatti, U.A.: Advance brain tumor segmentation using feature fusion methods with deep u-net model with cnn for mri data. *Journal of King Saud University-Computer and Information Sciences* **35**(9), 101793 (2023)
- [29] Nurfauzi, R., Nugroho, H.A., Ardiyanto, I., Frannita, E.L.: Autocorrection of lung boundary on 3d ct lung cancer images. *Journal of King Saud University-Computer and Information Sciences* **33**(5), 518–527 (2021)
- [30] O’Neil, A.Q., Kascenas, A., Henry, J., Wyeth, D., Shepherd, M., Beveridge, E., Clunie, L., Sansom, C., Seduikyte Keith Muir, E., Poole, I.: Attaining human-level performance with atlas location autocontext for anatomical landmark detection in 3d ct data. In: Proceedings of the European conference on computer vision (ECCV) Workshops (2018)
- [31] Payer, C., Štern, D., Bischof, H., Urschler, M.: Regressing heatmaps for multiple

- landmark localization using cnns. In: International conference on medical image computing and computer-assisted intervention. pp. 230–238. Springer (2016)
- [32] Payer, C., Štern, D., Bischof, H., Urschler, M.: Integrating spatial configuration into heatmap regression based cnns for landmark localization. *Medical image analysis* **54**, 207–219 (2019)
 - [33] Perakis, P., Passalis, G., Theoharis, T., Kakadiaris, I.A.: 3d facial landmark detection under large yaw and expression variations. *IEEE transactions on pattern analysis and machine intelligence* **35**(7), 1552–1564 (2012)
 - [34] Rudolph, D., Sinclair, P., Coggins, J.: Automatic computerized radiographic identification of cephalometric landmarks. *American Journal of Orthodontics and Dentofacial Orthopedics* **113**(2), 173–179 (1998)
 - [35] Rutoh, E.K., Guang, Q.Z., Bahadar, N., Raza, R., Hanif, M.S.: Gair-u-net: 3d guided attention inception residual u-net for brain tumor segmentation using multimodal mri images. *Journal of King Saud University-Computer and Information Sciences* p. 102086 (2024)
 - [36] Rutoh, E.K., Guang, Q.Z., Bahadar, N., Raza, R., Hanif, M.S.: Gair-u-net: 3d guided attention inception residual u-net for brain tumor segmentation using multimodal mri images. *Journal of King Saud University-Computer and Information Sciences* p. 102086 (2024)
 - [37] Saad, A., El-Bialy, A., Kandil, A., Sayed, A.: Automatic cephalometric analysis using active appearance model and simulated annealing. *ICGST Int J on Graphics, Vision and Image Processing, Special Issue on Image Retrieval and Representation* **6**, 51–67 (2006)
 - [38] Sabri, N., Hamed, H.N.A., Ibrahim, Z., Ibrahim, K., Isa, M.A., Diah, N.M.: The hybrid feature extraction method for classification of adolescence idiopathic scoliosis using evolving spiking neural network. *Journal of King Saud University-Computer and Information Sciences* **34**(10), 8899–8908 (2022)
 - [39] Shao, S., Yuan, X., Huang, Z., Qiu, Z., Wang, S., Zhou, K.: Diffuseexpand: Expanding dataset for 2d medical image segmentation using diffusion models. *arXiv preprint arXiv:2304.13416* (2023)
 - [40] Song, Q., Dai, Y., Lu, H., Jin, G.: High-throughput systolic array-based accelerator for hybrid transformer-cnn networks. *Journal of King Saud University-Computer and Information Sciences* **36**(8), 102194 (2024)
 - [41] Song, Q., Dai, Y., Lu, H., Jin, G.: High-throughput systolic array-based accelerator for hybrid transformer-cnn networks. *Journal of King Saud University-Computer and Information Sciences* **36**(8), 102194 (2024)
 - [42] Sun, K., Xiao, B., Liu, D., Wang, J.: Deep high-resolution representation learning for human pose estimation. In: *Proceedings of the IEEE/CVF conference on computer vision and pattern recognition*. pp. 5693–5703 (2019)
 - [43] Tan, Z., Madzin, H., Norafida, B., Rahmat, R.W.O., Khalid, F., Sulaiman, P.S.: Swinunelcst: Global–local spatial representation learning with hybrid cnn–transformer for efficient tuberculosis lung cavity weakly supervised semantic segmentation. *Journal of King Saud University-Computer and Information Sciences* **36**(4), 102012 (2024)

- [44] Upadhyay, P.K., Rastogi, S., Kumar, K.V.: Coherent convolution neural network based retinal disease detection using optical coherence tomographic images. *Journal of King Saud University-Computer and Information Sciences* **34**(10), 9688–9695 (2022)
- [45] Vaswani, A.: Attention is all you need. *Advances in Neural Information Processing Systems* (2017)
- [46] Wang, C.W., Huang, C.T., Hsieh, M.C., Li, C.H., Chang, S.W., Li, W.C., Vandaele, R., Marée, R., Jodogne, S., Geurts, P., et al.: Evaluation and comparison of anatomical landmark detection methods for cephalometric x-ray images: a grand challenge. *IEEE transactions on medical imaging* **34**(9), 1890–1900 (2015)
- [47] Wang, H., Liu, J., Tang, J., Wu, G.: Lightweight super-resolution head for human pose estimation. In: *Proceedings of the 31st ACM International Conference on Multimedia*. pp. 2353–2361 (2023)
- [48] Wen, X., Zhang, A., Lin, C., Pang, X.: Crnet: Cascaded refinement network for polyp segmentation. *Journal of King Saud University-Computer and Information Sciences* **36**(10), 102250 (2024)
- [49] Wu, C., Meng, G., Lian, J., Xu, J., Gao, M., Huang, C., Zhang, S., Zhang, Y., Yu, Y., Wang, H., et al.: A multi-stage ensemble network system to diagnose adolescent idiopathic scoliosis. *European Radiology* **32**(9), 5880–5889 (2022)
- [50] Yi, S., Chen, Z., Yi, L., She, F.: Cas: Breast cancer diagnosis framework based on lesion region recognition in ultrasound images. *Journal of King Saud University-Computer and Information Sciences* **35**(8), 101707 (2023)
- [51] Zhang, J., Liu, M., Wang, L., Chen, S., Yuan, P., Li, J., Shen, S.G.F., Tang, Z., Chen, K.C., Xia, J.J., Shen, D.: Context-guided fully convolutional networks for joint craniomaxillofacial bone segmentation and landmark digitization. *Medical image analysis* **60**, 101621 (2019), <https://api.semanticscholar.org/CorpusID:209166766>
- [52] Zhang, R., Mo, H., Hu, W., Jie, B., Xu, L., He, Y., Ke, J., Wang, J.: Super-resolution landmark detection networks for medical images. *Computers in Biology and Medicine* **182**, 109095 (2024)
- [53] Zhang, Z., Lu, Y., Ye, M., Huang, W., Jin, L., Zhang, G., Ge, Y., Baghban, A., Zhang, Q., Wang, H., et al.: A novel evolutionary ensemble prediction model using harmony search and stacking for diabetes diagnosis. *Journal of King Saud University-Computer and Information Sciences* **36**(1), 101873 (2024)
- [54] Zhao, J., Zhu, H., Niu, L.: Bitnet: a lightweight object detection network for real-time classroom behavior recognition with transformer and bi-directional pyramid network. *Journal of King Saud University-Computer and Information Sciences* **35**(8), 101670 (2023)
- [55] Zhao, M., Meng, N., Cheung, J.P.Y., Yu, C., Lu, P., Zhang, T.: Spinehrformer: A transformer-based deep learning model for automatic spine deformity assessment with prospective validation. *Bioengineering* **10**(11), 1333 (2023)
- [56] Zheng, Y., Liu, D., Georgescu, B., Nguyen, H., Comaniciu, D.: 3d deep learning for efficient and robust landmark detection in volumetric data. In: *Medical Image Computing and Computer-Assisted Intervention–MICCAI 2015: 18th International Conference, Munich, Germany, October 5–9, 2015, Proceedings, Part I* 18.

- pp. 565–572. Springer (2015)
- [57] Zhou, H.Y., Guo, J., Zhang, Y., Yu, L., Wang, L., Yu, Y.: nnformer: Interleaved transformer for volumetric segmentation. arXiv preprint arXiv:2109.03201 (2021)
 - [58] Zhou, S.K., Rueckert, D., Fichtinger, G.: Handbook of medical image computing and computer assisted intervention. Academic Press (2019)
 - [59] Zhu, H., Yao, Q., Zhou, S.K.: Datr: Domain-adaptive transformer for multi-domain landmark detection. arXiv preprint arXiv:2203.06433 (2022)
 - [60] Zhu, L., Wang, X., Ke, Z., Zhang, W., Lau, R.W.: Biformer: Vision transformer with bi-level routing attention. In: Proceedings of the IEEE/CVF conference on computer vision and pattern recognition. pp. 10323–10333 (2023)

Statements and Declarations

Funding

The authors declare that no funds, grants, or other support were received during the preparation of this manuscript.

Competing Interests

The authors declare that they have no known competing financial interests or personal relationships that could have appeared to influence the work reported in this paper.

Data Availability Statement

Data and code are already open-source.

Ethical approval

All procedures performed in studies involving human participants were in accordance with the ethical standards of the institutional and national research committee and with the 1964 Helsinki declaration and its later amendments or comparable ethical standards. The IRB approval is obtained.